doi: 10.82124/CEAS-GNC-2026-105 CEAS-GNC-2026-105

Electrodynamic Tethers in the Earth–Moon CR3BP: Stability Mapping under Lorentz Forcing

Elisa Velasco Romeo Master's Student, Universidad Carlos III de Madrid, Leganés, Spain.
100472189@alumnos.uc3m.es

Behrad Vatankhahghadim Visiting Professor, Universidad Carlos III de Madrid, Leganés, Spain.
bvatankh@ing.uc3m.es

ABSTRACT

Electrodynamic tethers (EDTs) are long, conductive wires or tapes deployed from spacecraft that enable energy generation and propellantless thrust when moving in a planetary magnetic field. This work extends a planar Earth–Moon Circular Restricted Three-Body Problem (CR3BP) model by including the EDT Lorentz force term with a controllable in-plane tether tilt relative to the local radial direction. Using dense grids of initial conditions, both local (around the five Lagrange points) and global (Earth–Moon synodic frame) escape-time and exit-basin stability maps are constructed to quantify how sustained EDT actuation influences stability patterns and transport pathways. Consistent with the expected results from the CR3BP, it is found that the large stable regions of the Earth–Moon system are not greatly affected by the EDT forcing. However, the exit patterns near the Earth display modified escape-time structures and altered transport routes. The addition of the Lorentz acceleration to the equations of motion enables adjustment of the tether current and tilt to target residence times near the collinear Lagrange points L1 and L2 and to manage leakage at the periphery of the triangular L4 and L5 points.

Keywords: Electrodynamic tethers, Circular Restricted Three-Body Problem, Lagrange points, Lorentz force, escape-time maps, exit-basin maps, tether tilt

1 Introduction

By moving through a planet's magnetized plasma, the relative motion of an electrodynamic tether (EDT) induces a voltage, known as a motional electromotive force (EMF), along its length, which in turn drives an electric current through the tether–plasma circuit and produces a Lorentz force on the current-carrying conductor. This enables propellantless, low-thrust actuation that trades electrical energy for orbital energy [1]. The Earth–Moon system is a compelling testbed because long dynamical timescales and weak dissipation make transport highly sensitive to small perturbations. At the same time, the ambient plasma provides a return path for current closure. In this work, the motion of the tether is modeled within the Circular Restricted Three-Body Problem (CR3BP) in the synodic (rotating) frame and the Lorentz acceleration from the tether current is then added to the equations of motion [2], [3], [4]. Within this framework we examine how sustained tether actuation influences transport and residence behavior near the Earth–Moon equilibria and in the global synodic frame.

From the 1960s onward, a series of tether experiments established feasibility and the underlying physics of tethered spacecraft systems [5]. NASA's Shuttle-based Tethered Satellite System missions (TSS-1 in 1992; TSS-1R in 1996) demonstrated the creation of a motional EMF and plasma-current collection in orbit; TSS-1R even produced higher-than-expected currents before the tether failure, highlighting challenges with arcing and mechanical stresses [6]. The Plasma Motor Generator (PMG, 1993) further showed an EDT can operate as an electrical generator in space [7]. A pivotal advance was the bare tether concept, which consists of an uninsulated wire acting as a distributed anode that can collect electrons along its length. This allowed for a great increase in current collection and overall efficiency. It was proposed by Sanmartín and Lorenzini and later pursued in NASA's (ultimately canceled) ProSEDS demonstration [5], [8].

Introducing EDTs into the CR3BP changes the Jacobi integral and adds a velocity-dependent, non-conservative perturbation. Early ESA-led studies (Peláez et al., 2008) showed that even modest EDT forcing can displace equilibria and alter stability regimes near the Earth–Moon Lagrange points [9]. Linear analyses around the perturbed equilibria characterized the resulting small-oscillation modes and suggested that tuning EDT intensity (via tether length or current) can marginally stabilize selected motions [10]. Later work introduced additional physics (tether elasticity [11], J2 perturbation, geomagnetic coupling), differentiating genuinely physical stability mechanisms from artificial modeling effects and motivating active control strategies to damp oscillations [12], [13].

As a baseline, previous studies found that for a radial tether (no tilt) the Lorentz term only slightly changes the main transport routes in the inner ring of long-lived motion surrounding the Earth and does not alter the overall stability structure around the Earth–Moon Lagrange points [14]. In other words, EDT actuation slightly favors existing transport channels, shifting ridges and exit biases while preserving the global manifold topology. Here that analysis is extended to a tilted tether whose in-plane orientation is controlled relative to the local radial direction. In this study, the planar CR3BP equations with Lorentz forcing and a fixed tilt angle are derived, and local and global stability maps for positive and negative current and an additional tilt angle are built. The results are interpreted in terms of residence-time shaping and transport-route modulation.

This paper is structured as follows. Section 2 presents the dynamical formulation of the planar Earth–Moon CR3BP and the Lorentz force term with a controllable in-plane tether tilt. Section 3 describes the construction of the escape-time and exit-basin stability maps together with the numerical integration and event definitions adopted for the simulations. Section 4 discusses the main results for different current polarities and for tilted configurations with $\theta = 30^\circ$ and 60°, highlighting the impact on residence-time shaping and transport pathways. Finally, Section 5 summarizes the key findings and outlines future research directions.

2 Dynamical Model

This section introduces the planar Earth–Moon CR3BP, the Lorentz-force model, the parametrization of the tether tilt, and the implications for the Jacobi integral and Hill curves.

2.1 Planar Earth–Moon CR3BP

As is known, the general three-body problem has no analytical solution due to its chaotic behavior. The motion is modeled within the planar CR3BP (PCR3BP), a framework that offers a solvable and insightful representation under the following assumptions: the two primary bodies (Earth and Moon) move in circular orbits about their common barycenter; the third body m, of negligible mass compared to the other two ($m \ll M_1, M_2$), does not influence their dynamics; and the motion is restricted to the plane, meaning $z = 0$. In the synodic frame, the two primary masses M_1 (e.g., Earth) and M_2 (e.g., Moon) are

fixed on the x-axis at $-r_1$ and r_2, respectively. The Earth–Moon separation distance is given by a, such that $r_1 + r_2 = a$.

The frame rotates with constant angular velocity ω, given by [15]

$$\omega^2 = \frac{G\,(M_1 + M_2)}{a^3}, \tag{1}$$

so that the two primaries perform a circular relative motion of radius r_1 and r_2 about the origin of the synodic frame (Figure 2). G represents the universal gravitational constant. In practice, the transformation from the ECI frame to the synodic frame (CR) is carried out by a single rotation about the z-axis through the angle $\phi(t) = \omega t$, as shown in Figure 1.

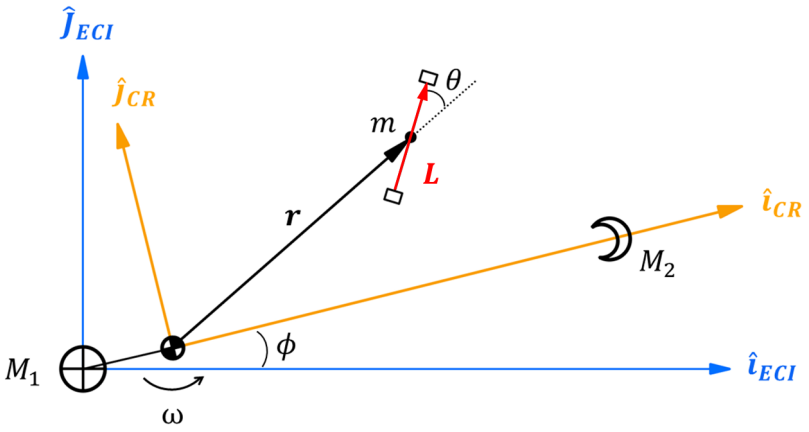

Fig. 1 ECI frame, rotating frame and tether tilt angle θ with respect to the local radial direction.

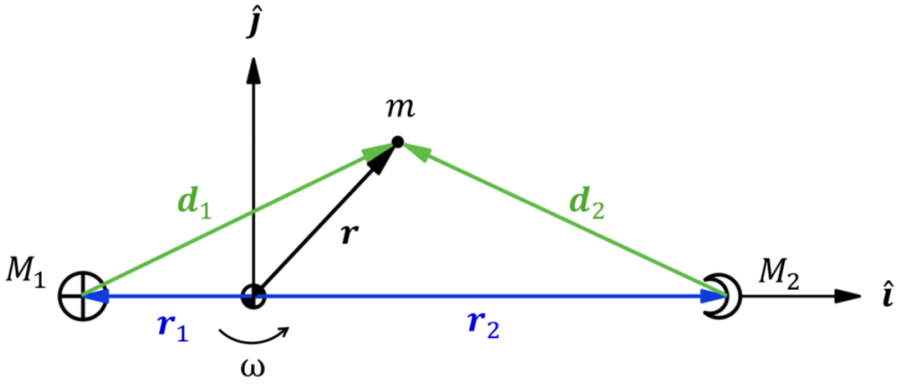

Fig. 2 Synodic rotating frame of the Earth–Moon CR3BP.

Let (x, y) be the dimensional synodic coordinates of the EDT-equipped spacecraft measured from the barycenter. The planar equations of motion of the spacecraft in the rotating frame including the Lorentz term are [15]

$$\begin{cases} \ddot{x} - 2\omega\dot{y} - \omega^2 x = -\dfrac{GM_1}{d_1^3}(x + r_1) - \dfrac{GM_2}{d_2^3}(x - r_2) + a_{L,x} \\ \ddot{y} + 2\omega\dot{x} - \omega^2 y = -\dfrac{GM_1}{d_1^3}y - \dfrac{GM_2}{d_2^3}y + a_{L,y}, \end{cases} \tag{2}$$

where d_1 and d_2 are the distances between the EDT and the two primaries (Figure 2). The terms $a_{L,x}$ and $a_{L,y}$ represent the Lorentz acceleration produced by the electrodynamic tether.

2.2 Lorentz forcing and magnetic field

The electrodynamic tether (EDT) acceleration is computed in the Earth-Centered Inertial (ECI) frame and then mapped into the synodic (co-rotating) frame, where the CR3BP equations of motion are integrated. At time t, the transformation between frames is performed through a rotation about the z-axis by the angle $\phi(t) = \omega t$, such that $R_{\mathrm{ECI}\to\mathrm{CR}} = R_z(\phi)$ and $R_{\mathrm{CR}\to\mathrm{ECI}} = R_z(-\phi)$. All physical vectors required to evaluate the Lorentz acceleration are first constructed in the ECI frame and then rotated back to the synodic frame for superposition with the gravitational, Coriolis, and centrifugal terms.

The Lorentz force acting on a straight, current-carrying tether is given by

$$\mathbf{F}_L = I\,\mathbf{L}\times\mathbf{B}, \tag{3}$$

where I is the tether current, $\mathbf{L} = L\,\hat{\mathbf{u}}_L$ encodes the tether length and orientation (Figure 1), and $\mathbf{B}$ is the geomagnetic field of the Earth. The corresponding acceleration used in the equations of motion is

$$\mathbf{a}_{L,\mathrm{ECI}} = \frac{I}{m_t}\,\mathbf{L}_{\mathrm{ECI}}\times\mathbf{B}_{\mathrm{ECI}}(\mathbf{r}_{\mathrm{ECI}}), \qquad \mathbf{a}_L = R_{\mathrm{ECI}\to\mathrm{CR}}\,\mathbf{a}_{L,\mathrm{ECI}}. \tag{4}$$

In the synodic frame of the Earth–Moon CR3BP, a geomagnetic dipole with nonzero tilt becomes time-dependent due to the relative rotation between the Earth-fixed magnetic axis and the rotating frame. This introduces periodic variations in the Lorentz acceleration, complicating the analysis and interpretation of the main dynamic behavior.

In the present work, a reduced-order framework based on the Hill approximation of the circular restricted three-body problem is adopted [16]. In this formulation, spatial variables in the vicinity of the Earth are scaled with the characteristic parameter $\nu^{1/3}$, where ν is the mass ratio of the Earth–Moon system, and the magnetic field can be formally expanded about the Earth as

$$\mathbf{B} = \mathbf{B}^{(0)} + \nu^{1/3}\,\mathbf{B}^{(1)} + O(\nu^{2/3}), \tag{5}$$

where $\mathbf{B}^{(0)}$ represents the magnetic field evaluated at the Earth position and the higher-order terms account for spatial variations of the field.

The full dipole field is given by [9]

$$\mathbf{B}(\mathbf{r}) = \mu_m\left(\frac{R_E}{r}\right)^3\left[3(\hat{\mathbf{m}}\cdot\hat{\mathbf{r}})\,\hat{\mathbf{r}} - \hat{\mathbf{m}}\right] = \frac{\mu_0}{4\pi\|\mathbf{r}\|^5}\left[3(\mathbf{m}\cdot\mathbf{r})\,\mathbf{r} - \|\mathbf{r}\|^2\mathbf{m}\right], \tag{6}$$

where $\hat{\mathbf{m}}$ is the unit vector along the magnetic dipole axis, $\hat{\mathbf{r}} = \mathbf{r}/\|\mathbf{r}\|$, R_E is the Earth's radius, and μ_m is a reference dipole-field magnitude. This expression captures the spatial dependence of the geomagnetic field, whose magnitude decreases with distance from the Earth and whose direction varies with position.

For completeness, a commonly used simplification consists of retaining only the leading-order contribution in the expansion, yielding the uniform-field model

$$\mathbf{B} = -B_0\,\hat{\mathbf{k}}, \tag{7}$$

where $\hat{\mathbf{k}}$ is the unit vector normal to the synodic plane and B_0 is a constant reference magnetic field magnitude. This approximation is often adopted to simplify the analysis, as it removes spatial variability and reduces the Lorentz acceleration to a uniform perturbation.

However, in the present study the full position-dependent dipole field given by Eq. (6) is retained in the numerical simulations. This allows the Lorentz acceleration to reflect the spatial variation of the geomagnetic field, which is stronger near the Earth and decreases with distance, leading to a non-

uniform perturbation of the CR3BP dynamics across the domain. This formulation preserves the physical consistency of the model while maintaining sufficient simplicity to analyze the impact of Lorentz forcing on transport and stability in the Earth–Moon system.

2.3 Controllable in-plane tether tilt

The in-plane orientation of the tether is parametrized by a fixed angle θ relative to the local radial direction $\hat{\mathbf{e}}_r$ in the rotating frame such that

$$\hat{\mathbf{u}}_L = \cos\theta\,\hat{\mathbf{e}}_r + \sin\theta\,\hat{\mathbf{e}}_\tau, \qquad \hat{\mathbf{e}}_r = \frac{\mathbf{r}}{\|\mathbf{r}\|}, \quad \hat{\mathbf{e}}_\tau = \frac{\boldsymbol{\omega}}{\|\boldsymbol{\omega}\|} \times \hat{\mathbf{e}}_r. \tag{8}$$

The tether length vector used in the Lorentz term is then

$$\mathbf{L}_{\mathrm{ECI}} = L\, R_{CR\to\mathrm{ECI}}\big(\hat{\mathbf{u}}_L\big).$$

This ensures that the tilt angle θ is applied relative to the local radial direction, as illustrated in Figure 1.

The cross product in Eq. (3) ensures that the acceleration is always perpendicular to both the tether axis and the magnetic field, and the tilt angle θ determines how much of this acceleration projects onto the local radial and along-track directions. The configuration that maximizes the Lorentz force magnitude on the along-track direction is the one in which **L** and **B** are perpendicular. In the present planar setting, the radial orientation provides the reference case against which tilted configurations are compared.

2.4 Jacobi integral and Hill curves under Lorentz forcing

In the rotating frame of the planar CR3BP, the effective potential is [17]

$$U(x, y) = \frac{GM_1}{r_1} + \frac{GM_2}{r_2} + \frac{1}{2}\,\omega^2\,(x^2 + y^2), \tag{9}$$

and the Jacobi integral takes the form [18]

$$C = 2U(x, y) - \big(\dot{x}^2 + \dot{y}^2\big). \tag{10}$$

Contours of constant C define the zero-velocity (Hill's) curves via $2U(x, y) = C$. These zero-velocity contours define allowed regions of motion, where $2U(x, y) \geq C$. In other words, the test particle cannot enter domains with $2U(x, y) < C$, which would require an imaginary speed. For each Lagrange point, the corresponding Jacobi level $C_{L_i} = 2U(x_{L_i}, y_{L_i})$ passes through the familiar "necks" that connect the primary lobes to the exterior region; decreasing C opens these bottlenecks, whereas increasing C closes them.

In the unforced CR3BP, C is conserved. When a non-conservative acceleration such as the tether's Lorentz term is present, C varies along the trajectory. Therefore, EDT actuation should not be interpreted as imposing a single new Jacobi level, but rather as locally reweighting the accessibility of transport channels over time. This viewpoint is consistent with the stability maps presented later: the Lorentz term modifies residence times and exit preferences without changing the underlying manifold topology.

3 Methodology

This section describes the construction of the stability maps, the definition of initial conditions and events, and the numerical integration procedure.

3.1 Stability metrics: escape-time and exit-basin maps

In this study, the stability region is defined as any initial condition that does not trigger an event by a fixed, mission-relevant time horizon. The possible events that can be encountered when propagating the trajectory of the tether are collision with the Earth, collision with the Moon, or crossing a bounding box (escape). This finite-time "stability" is quantified using two complementary maps:

- **Escape-time map:** For each initial condition (IC) on a 2-D grid, we integrate forward the equations of motion (2) until an exit event is detected or until the horizon $T_{\max}$ is reached. Color encodes time-to-exit T_{esc}; bright yellow identifies long-lived invariant structures, while dark blue represents short escape times, meaning very unstable regions.
- **Exit-basin map:** Each IC is colored by its first outcome, revealing the structure of transport pathways and their sensitivity to initial conditions, as commonly studied in chaotic scattering and basin analysis [19].

3.2 Initial conditions, grids, and events

Local Cartesian grids of planar offsets $(\Delta x, \Delta y)$ are defined around each Lagrange point (x_{L_i}, y_{L_i}) with zero rotating-frame velocity to isolate geometry-driven effects. Each initial condition (IC) is therefore

$$\mathbf{X}_0 = \big(x_{L_i} + \Delta x,\ y_{L_i} + \Delta y,\ \dot{x}_0,\ \dot{y}_0\big), \qquad (\dot{x}_0, \dot{y}_0) = (0, 0).$$

The current magnitude to be tested is fixed as $I_{\text{tether}} = \pm 100$ A. Although it is higher than typical passive collection levels, it is selected here to enhance the visibility of the Lorentz-induced dynamical effects. The integration horizon is set to $T_{\max} = 2.0 \times 10^7$ s to capture long-term cislunar dynamics while remaining computationally tractable. For each libration point, a bounded box of half-width $R_{\text{box}} = 1 \times 10^8$ m is defined and applied uniformly across all regions, ensuring consistency between maps.

To reveal large-scale transport, the global maps assemble tiles placed at the absolute synodic coordinates over a large Earth–Moon box. Each initial state is integrated forward in time under the full dynamical model, and the corresponding escape time T_{esc} is recorded. After repeating this procedure for each current, the resulting tiles are placed back into their correct absolute positions in the synodic x–y frame using a common color scale.

Integration halts at the earliest of:

1) **Collision with a primary:** (x, y) enters a disk of radius $3R_E$ (Earth) or $3R_M$ (Moon) centered at the corresponding primary.
2) **Domain escape:** (x, y) crosses the boundary of the global box with half-width 7×10^8 m.
3) **Time horizon:** $t = T_{\max}$.

Each IC is labeled according to its first event. In addition, the exact time at which the first exit event occurs is recorded to create the escape-time maps.

3.3 Numerical integration and implementation

Trajectory integration is performed using MATLAB's `ode113` with relative and absolute tolerances of 10^{-7} and 10^{-9}, respectively. The tether tilt angle θ is implemented in the equations of motion (Equation 2) as a fixed in-plane rotation of the tether direction vector relative to the local radial direction. In the corresponding MATLAB function, the unit tether vector is defined as $\hat{\mathbf{u}}_L = \cos\theta\,\hat{\mathbf{e}}_r + \sin\theta\,\hat{\mathbf{e}}_\tau$, which is then transformed to the inertial frame to compute the Lorentz acceleration $\mathbf{a}_L = (I/m_t)(\mathbf{L} \times \mathbf{B})$.

For each combination of current polarity, tilt angle and initial-condition grid, trajectories are propagated and classified according to their first exit event. The resulting data are then assembled onto the corresponding grid to construct the escape-time and exit-basin maps.

4 Results

This section first introduces the tether parameters adopted in the simulations and then presents the local and global stability maps for the no-tilt and tilted cases.

4.1 Simulation parameters

The EDT model used in this study is intentionally simplified in order to emphasize the dynamical role of Lorentz forcing within the planar Earth–Moon CR3BP. The tether is represented as a straight, rigid conductor of constant length $L = 20$ km (similar to that used in the TSS-1 mission of 1992 [6]) and lumped mass $m = 20$ kg, at the lower end of typical tether-satellite values [20]. The current is treated as a control parameter fixed at $I = \pm 100$ A. Although this current magnitude exceeds typical passive collection capabilities, it is deliberately chosen to amplify the Lorentz acceleration and make its influence on the CR3BP transport structures clearly observable.

4.2 Effect of current for the radial tether ($\theta = 0°$)

This subsection analyzes the effect of current polarity on the stability maps for the radial tether configuration. The response is first examined locally around the Lagrange points and then at the global scale to assess changes in transport structure.

4.2.1 Local response near the collinear points (L_1, L_2, L_3)

Local maps around the collinear Lagrange points display the expected thin, elongated ridges of high T_{esc}, corresponding to motion organized by the stable manifolds of nearby periodic orbits. This is consistent with the saddle-type character of the collinear equilibria in the classical CR3BP.

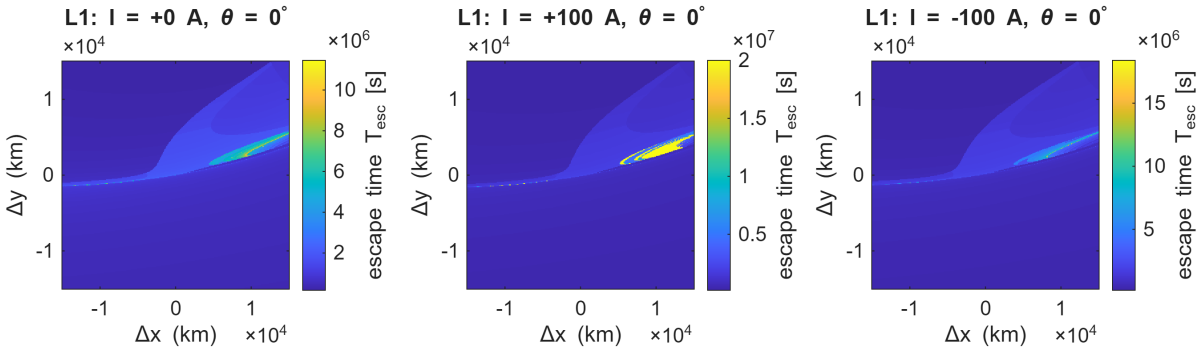

Fig. 3 L_1: Local escape-time stability map ($\theta = 0°$).

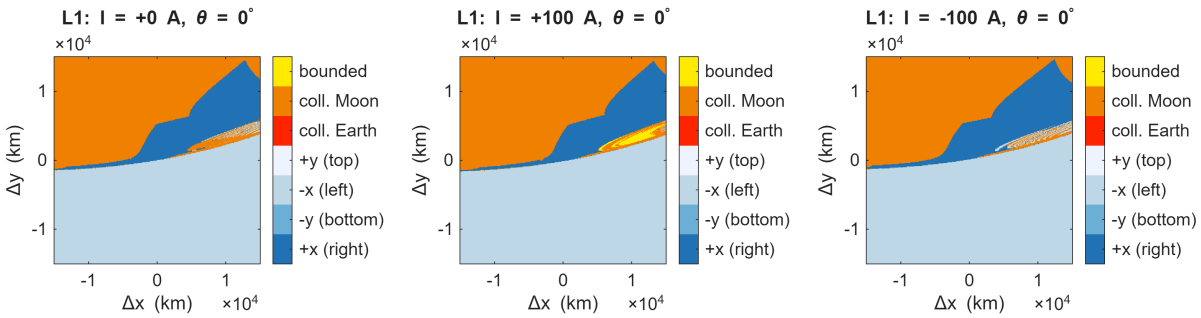

Fig. 4 L_1: Local exit-basin stability map ($\theta = 0°$).

Around L_1, the unforced case already shows a narrow high-T_{esc} filament embedded in a broader region of rapid escape. When radial EDT forcing is introduced, the overall structure of the filament remains, but its properties change in a clearly sign-dependent manner. For positive current ($I = +100$ A), the high-T_{esc} ridge becomes sharper, wider, and more intense, with a noticeably larger yellow region and higher maximum escape times. In contrast, for negative current ($I = -100$ A), the ridge weakens and the surrounding region of rapid escape expands, indicating a reduction in local stability.

The corresponding exit-basin maps exhibit very similar geometric patterns in all cases, confirming that the underlying transport structure is preserved. The main differences lie in the central long-lived regions that separate the different outcomes, consistently with the previous maps. So the role of the EDT here is mainly to reweight the access to pre-existing transport routes rather than to create new ones.

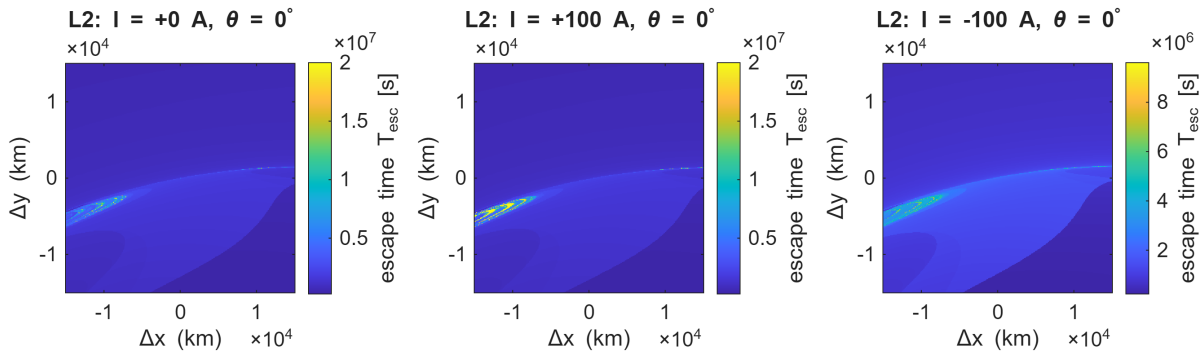

Fig. 5 L_2**: Local escape-time stability map** ($\theta = 0°$).

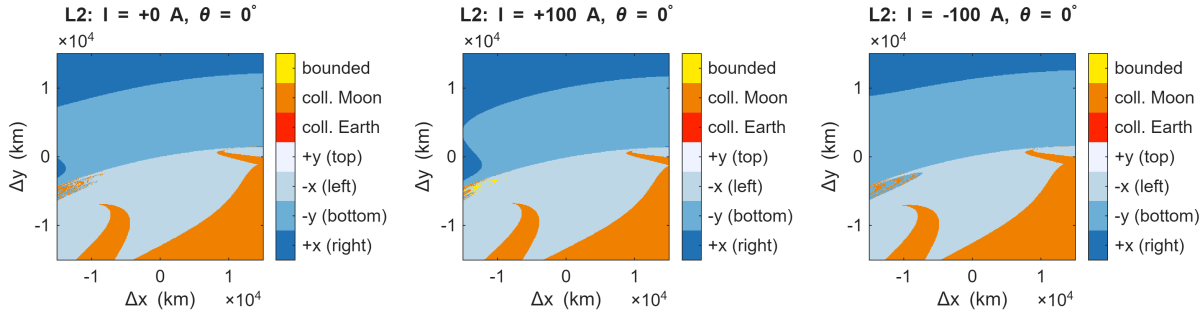

Fig. 6 L_2**: Local exit-basin stability map** ($\theta = 0°$).

The response near L_2 follows the same overall pattern, but with less intensity. The long-lived ridge remains present in all cases, with only modest sharpening for $I = +100$ A and slight weakening for $I = -100$ A. The changes are mainly confined to the ridge core and nearby transition regions, indicating a similar but less pronounced sensitivity to EDT forcing compared to L_1. This weaker response reflects the fact that the Lorentz perturbation couples less effectively with the local manifold structure around L_2, and therefore produces only modest changes in residence time and basin geometry.

Near L_3 (Figure 7 and Figure 8), the unforced case exhibits an almost horizontal, very thin strip of large T_{esc}, consistent with a very narrow long-lived region. When radial EDT forcing is introduced, the Lorentz acceleration acts locally as a vertical bias in the $(\Delta x, \Delta y)$ plane, so the strip is displaced in a sign-dependent way: upward for $I = +100$ A and downward for $I = -100$ A. Moreover, the strip becomes more diffuse and its maximum escape times decrease noticeably. This indicates that the forcing does not create a new long-lived set, but rather pushes trajectories away from the thin long-lived region, resulting in shorter residence times. The asymmetry of the perturbed strip, with one sharp edge and one progressively blended side, reflects the breaking of the near-symmetry of the unforced problem: the Lorentz term introduces a preferred transverse drift, producing abrupt loss of residence on one side of the strip and more gradual leakage on the other. Reversing the current reverses this asymmetry.

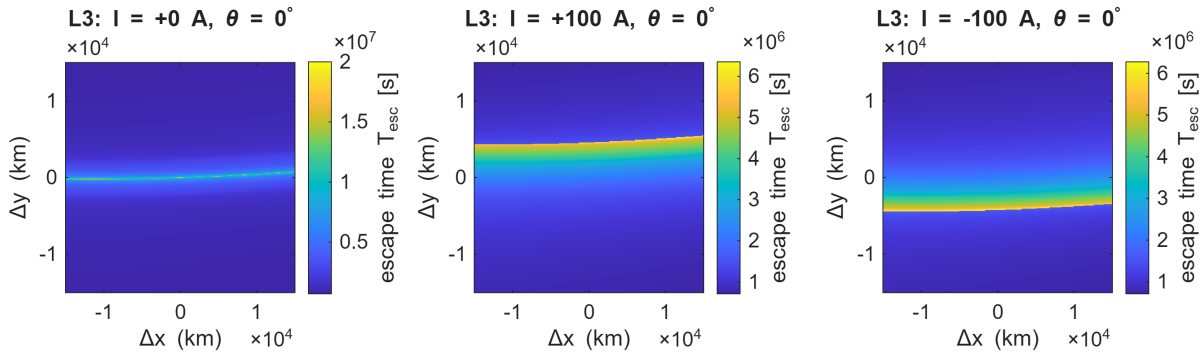

Fig. 7 L_3**: Local escape-time stability map** ($\theta = 0°$).

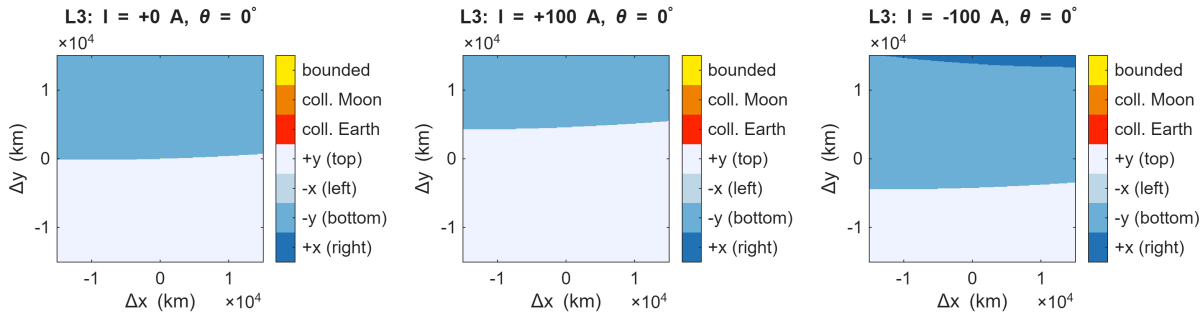

Fig. 8 L_3**: Local exit-basin stability map** ($\theta = 0°$).

4.2.2 Local response near the triangular points (L_4, L_5)

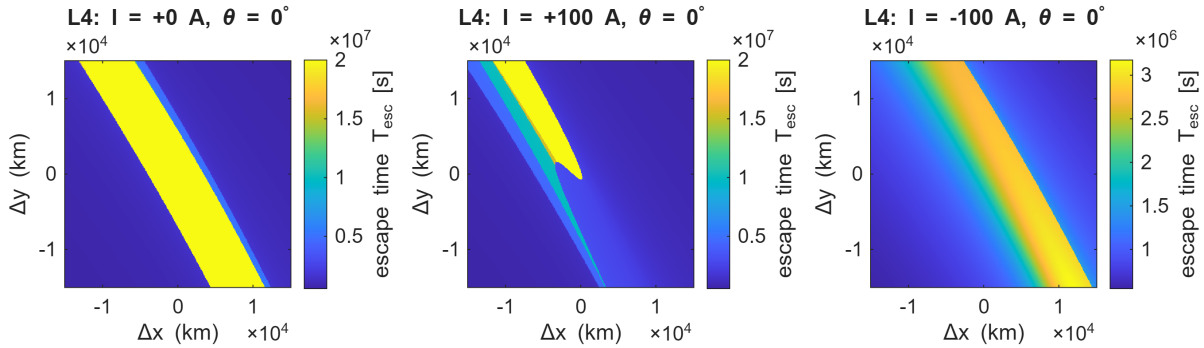

Fig. 9 L_4**: Local escape-time stability map** ($\theta = 0°$).

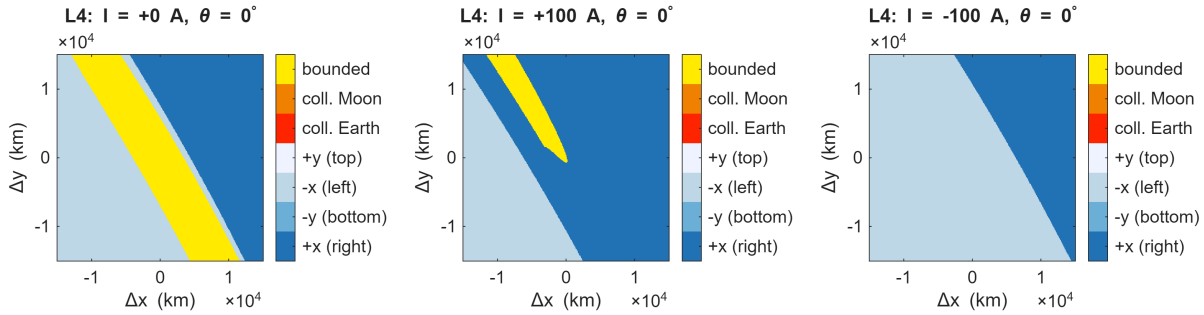

Fig. 10 L_4**: Local exit-basin stability map** ($\theta = 0°$).

The triangular points show a much stronger dependence on current polarity than the collinear points. In the unforced case, both L_4 and L_5 exhibit broad diagonal bands of large T_{esc}, and the exit-basin maps confirm that most of these regions are bounded up to the chosen time horizon, consistent with the classical tadpole-like stability of the triangular Lagrange points.

Once radial EDT forcing is introduced, the broad long-lived structure remains, but becomes strongly polarity-dependent. Around L_4 (Figure 9 and Figure 10), $I = +100$ A preserves only a shortened bounded wedge in the upper part of the original band. For $I = -100$ A, the change is even stronger: the exit-basin map shows that the bounded region is essentially lost, even though the escape-time map still shows a broad diagonal strip of elevated residence times.

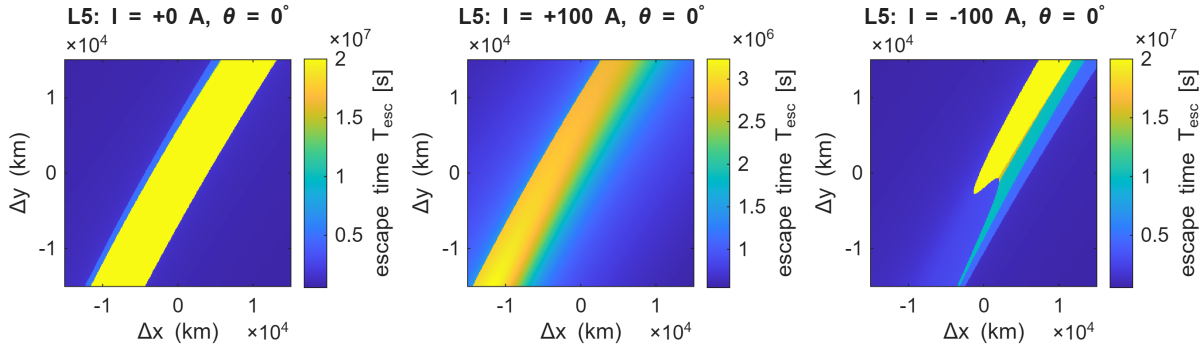

Fig. 11 L_5**: Local escape-time stability map** ($\theta = 0°$)**.**

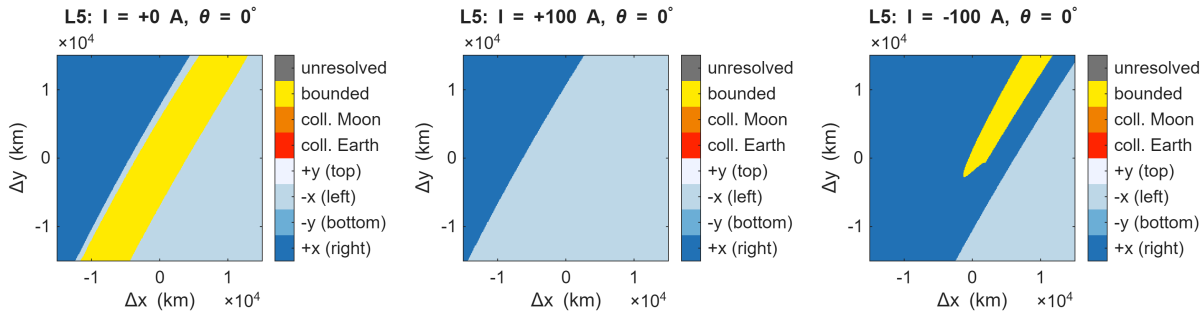

Fig. 12 L_5**: Local exit-basin stability map** ($\theta = 0°$)**.**

Around L_5 (Figure 11 and Figure 12), the opposite trend is observed: $I = +100$ A strongly weakens the bounded band, while $I = -100$ A preserves a compact bounded wedge. This behavior is consistent with the geometric symmetry of the Earth–Moon CR3BP, in which L_4 and L_5 are mirror images with respect to the x-axis. In the unforced case, this symmetry is reflected in the maps. When Lorentz forcing is introduced, the symmetry is preserved only if the current polarity is also reversed, since the direction of the acceleration depends on the sign of the cross product $\mathbf{L} \times \mathbf{B}$. As a result, the maps for $(L_4, +100\,\text{A})$ and $(L_5, -100\,\text{A})$, and vice versa, become mirror counterparts. This behavior follows directly from the geometry of the problem and is fully consistent with the mathematical structure of the equations of motion.

An important observation is that high escape times do not necessarily correspond to bounded motion. In several forced cases, the escape-time maps display broad long-lived strips, while the exit-basin maps show that these trajectories eventually escape before the time horizon. Overall, EDT actuation tends to reduce the extent of genuinely bounded regions around the triangular Lagrange points, increasing leakage from the stable bands and weakening their effective stability, even when long residence times are still observed.

4.2.3 Global stability and transport structure

Figure 13–Figure 15 show the global escape-time and exit-basin maps for the radial tether configuration, $\theta = 0°$, and $I = 0, \pm 100$ A. In the unforced case, the escape-time map displays a broad Earth-centered ring of long-lived trajectories, surrounded by thin ridges and a Moon-side lobe. The corresponding exit-basin map confirms that a large fraction of this ring is genuinely bounded up to $T_{\max}$, lying between the central Earth-collision region and the outer escape basins. In the classical CR3BP, this picture is naturally related to the Hill regions and the transport bottlenecks associated with the Jacobi integral: long-lived motion is organized by manifold-guided channels, while the Moon-side lobe marks the main opening toward the exterior.

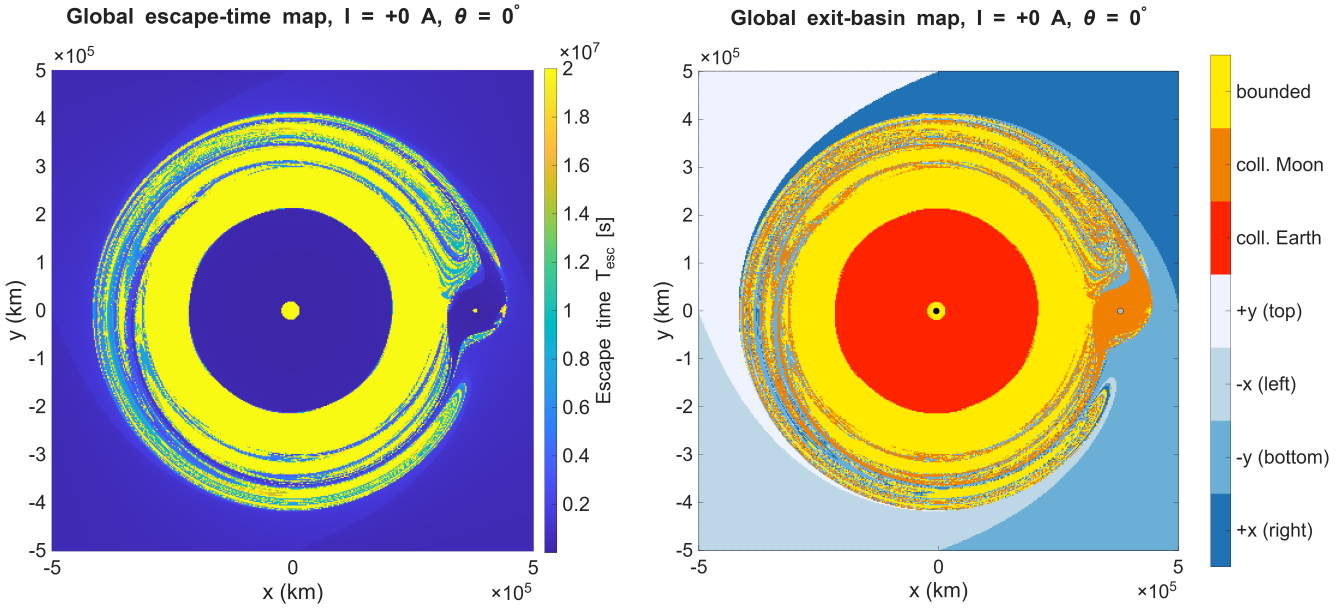

(a) Escape-time map **(b) Exit-basin map**

Fig. 13 Global maps for $I = 0$ A ($\theta = 0°$).

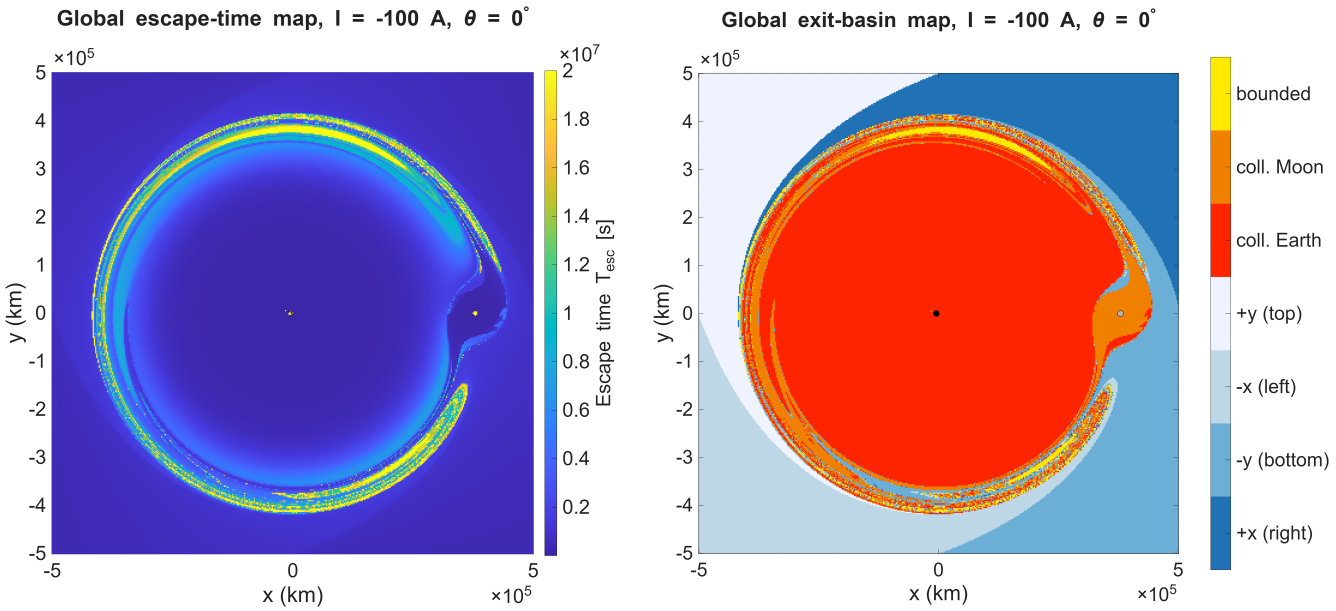

(a) Escape-time map **(b) Exit-basin map**

Fig. 14 Global maps for $I = -100$ A ($\theta = 0°$).

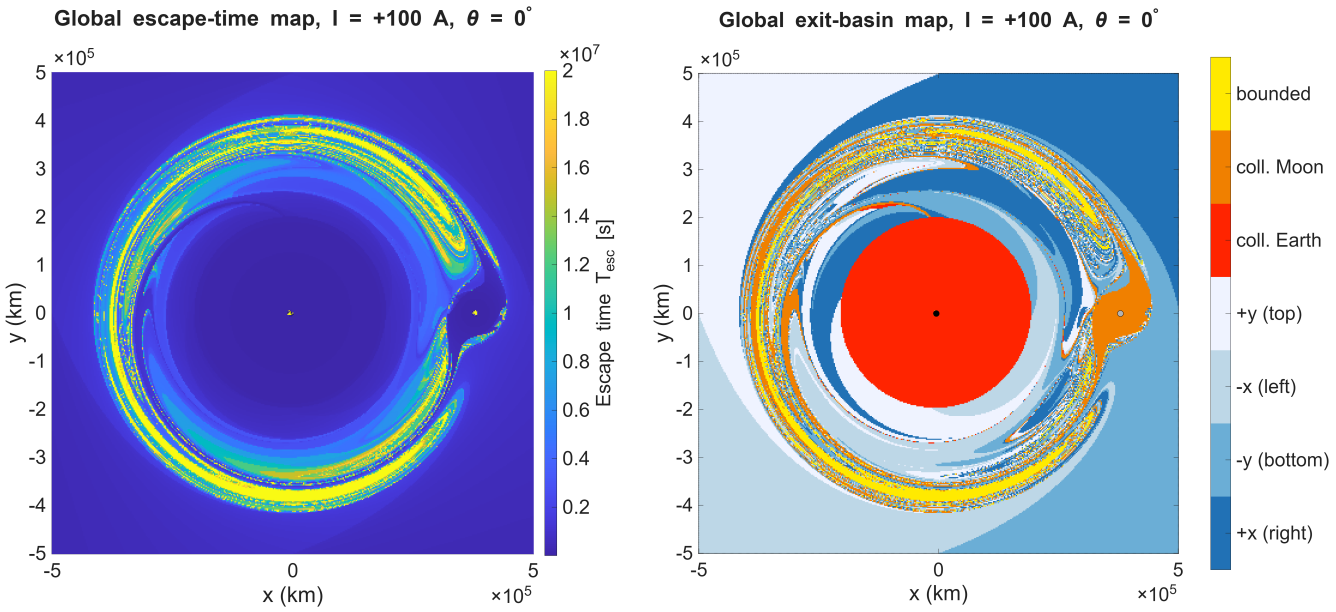

(a) Escape-time map **(b) Exit-basin map**

Fig. 15 Global maps for $I = +100$ A ($\theta = 0°$).

When radial EDT forcing is introduced, this large-scale structure is not destroyed. The outer ring of long-lived ridges and the Moon-side lobe remain in approximately the same location, indicating that the global CR3BP transport structure is preserved. However, the broad bounded ring around the Earth is strongly reduced, and the effect depends clearly on the current polarity.

For $I = -100$ A, the broad circular band is lost, and most of the affected region is redirected toward collision with the Earth rather than toward escape through the box boundaries. For $I = +100$ A, the effect is different: the escape-time map becomes more layered and filamentary in the inner circle, and the exit-basin map shows that much of the bounded region present for $I = 0$ is replaced by escape trajectories. In this sense, positive current increases the accessibility of the pre-existing transport channels that connect the inner ring with the outer escape channels. Thus, both current polarities reduce finite-time boundedness near the Earth, but they do so in different ways: negative current strongly enlarges the Earth-impact basin, whereas positive current favors outward transport.

These changes can be interpreted qualitatively in terms of the Jacobi integral and Hill regions framework. In the unforced CR3BP, decreasing the Jacobi constant opens the necks and increasing it closes them. In the forced problem, however, the Lorentz term makes the Jacobi integral time-dependent, so the system does not correspond to a single fixed energy level. Instead, EDT actuation modifies how trajectories access the existing transport channels over time. In particular, negative current effectively closes the available escape routes by shrinking the Hill region surrounding the Earth, confining trajectories and redirecting them toward impact. Conversely, positive current opens the necks, increasing the accessibility of the transport channels and allowing a large fraction of trajectories that were originally bounded to escape. The effect of current is most pronounced in the Earth-centered inner ring, where bounded motion is significantly reduced. This behavior is also consistent with the dipole nature of the geomagnetic field, whose magnitude decreases with distance from the Earth, leading to stronger Lorentz forcing in the inner region.

Taken together, the collinear-point maps show that radial EDT forcing modifies all regions while preserving their saddle-type structure, with the strongest effect near L_1, weaker near L_2, and a distinct displacement and weakening at L_3. At the triangular points, the effect is stronger and depends on current polarity, generally reducing the size of the stable regions. Overall, radial EDT actuation preserves

the global transport topology but redistributes residence times and enhances leakage, especially in the Earth-centered ring and near L_4 and L_5.

4.3 Effect of tilt angle relative to local radial orientation

This subsection analyzes the effect of the tether tilt angle for a fixed positive current, $I = +100$ A. The response is first examined locally around the Lagrange points and then at the global scale to assess how reorienting the tether redistributes the Lorentz forcing within the transport structure of the Earth–Moon CR3BP.

4.3.1 Local response near the collinear points (L_1, L_2, L_3)

With increasing tilt, the Lorentz acceleration is redistributed between radial and along-track components. In the collinear-point maps, this does not change the base structure, but it does modify the sharpness and extent of the long-lived regions.

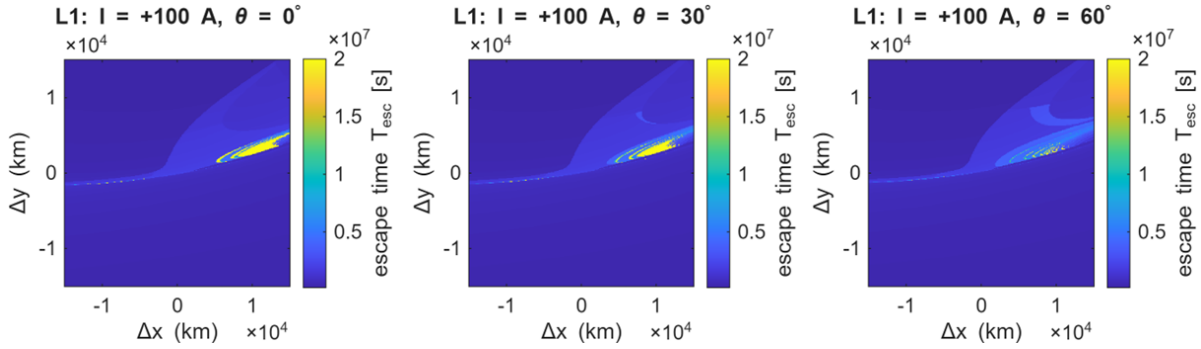

Fig. 16 L_1: Local escape-time stability map ($I = +100$ A).

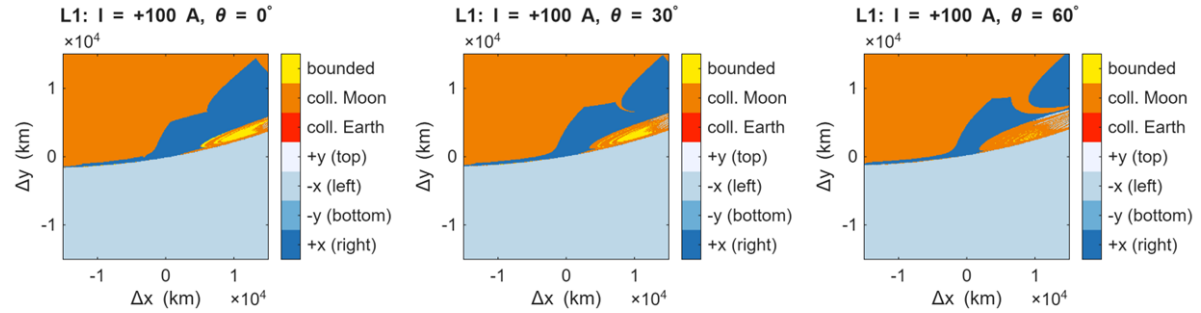

Fig. 17 L_1: Local exit-basin stability map ($I = +100$ A).

Around L_1, the narrow high-T_{esc} filament remains present for all tilt angles. For $\theta = 30°$, the changes are modest, with a slight redistribution of residence times around the main ridge. For $\theta = 60°$, the ridge is still clearly identifiable, but the extent of the long-residence-time region is noticeably reduced, and the surrounding transition region becomes more diffuse. This reduction is likely associated with the fact that, for larger tilt angles, the Lorentz acceleration is no longer predominantly aligned with the along-track direction, weakening its ability to sustain long-lived motion along the filament. This trend is also clearly reflected in the exit-basin maps, where the yellow regions progressively shrink as the tilt angle increases, consistently indicating a reduction in bounded motion.

The response near L_2 (Figure 18 and Figure 19) is weaker. The long-lived ridge persists in nearly the same location for all three tilt angles, and only small changes are observed in the ridge core intensity and in the neighboring transition regions. The corresponding exit-basin maps remain very similar, again indicating that the Lorentz perturbation couples only weakly with the local manifold geometry around L_2.

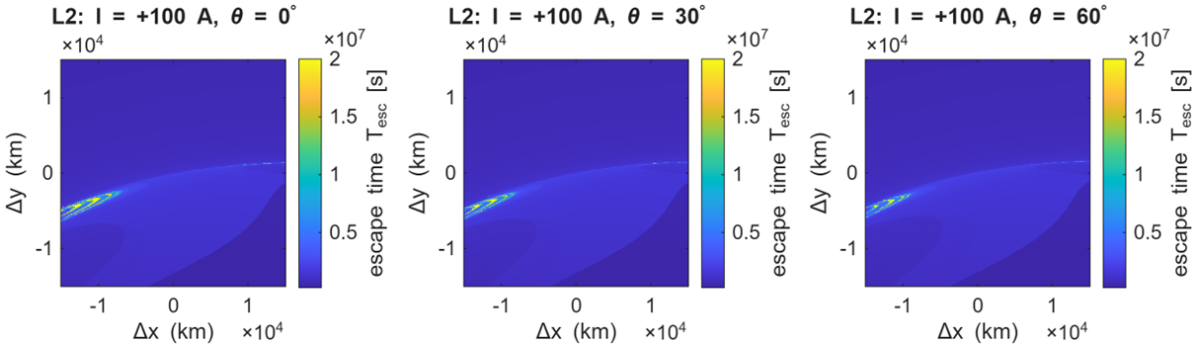

Fig. 18 L_2**: Local escape-time stability map (**$I = +100$ **A).**

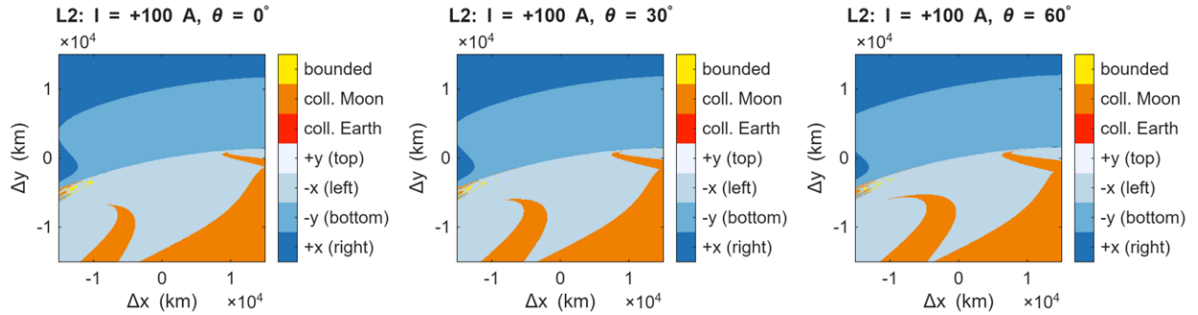

Fig. 19 L_2**: Local exit-basin stability map (**$I = +100$ **A).**

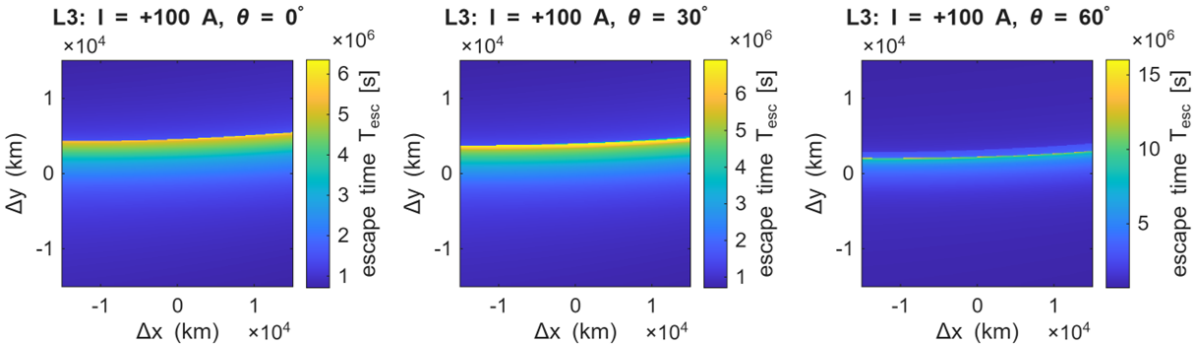

Fig. 20 L_3**: Local escape-time stability map (**$I = +100$ **A).**

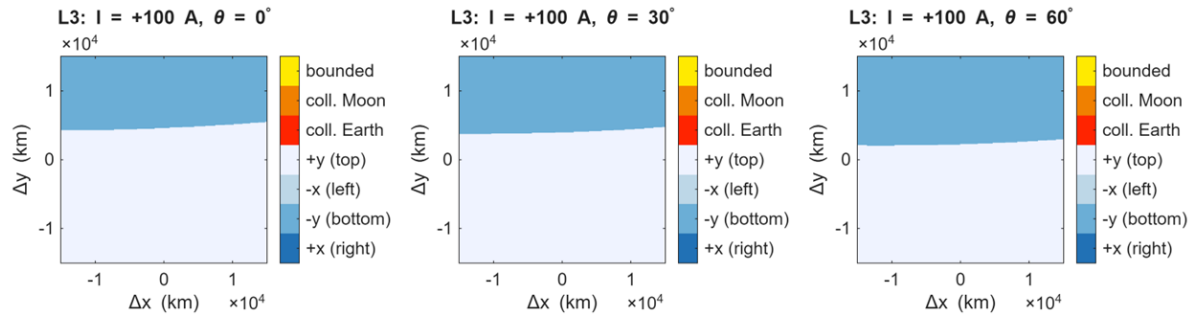

Fig. 21 L_3**: Local exit-basin stability map (**$I = +100$ **A).**

Near L_3, the thin long-lived strip also remains present for all tilt angles, but its response is more specific. From $\theta = 0°$ to $\theta = 30°$, the strip becomes slightly more concentrated and its maximum escape times increase. For $\theta = 60°$, this trend is reinforced: the strip narrows further and exhibits even higher T_{esc} values, while the exit-basin structure remains almost unchanged. This behavior suggests that increasing tilt aligns the Lorentz acceleration more favorably with the local direction of the long-lived structure, reducing transverse dispersion and allowing trajectories to remain confined to the strip for longer times.

4.3.2 *Local response near the triangular points (L_4, L_5)*

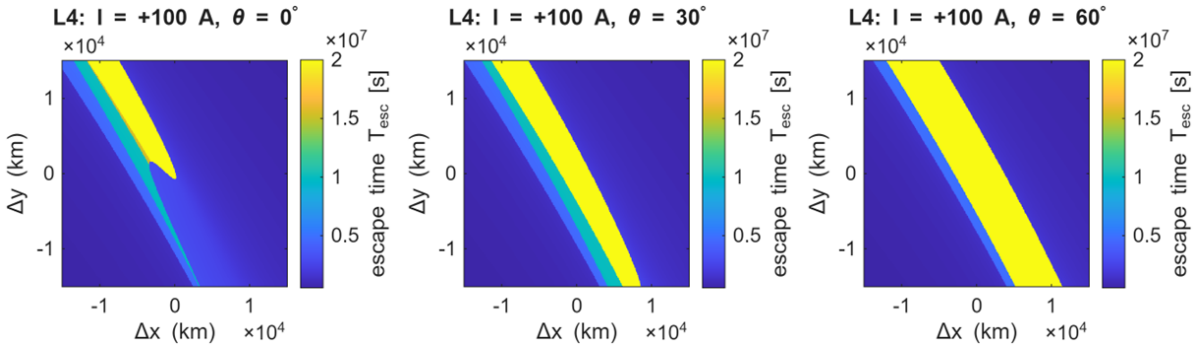

Fig. 22 L_4**: Local escape-time stability map (**$I = +100$ **A).**

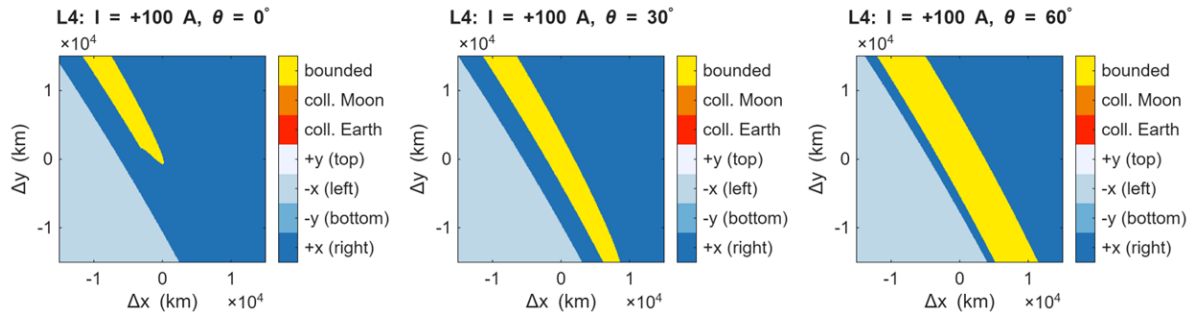

Fig. 23 L_4**: Local exit-basin stability map (**$I = +100$ **A).**

The triangular points are more sensitive to tilt than the collinear points. Around L_4, the $\theta = 0°$ case retains only the shortened bounded wedge already observed for the radial tether. Interestingly, as the tilt increases, the local stability is progressively recovered. For $\theta = 30°$, the bounded band broadens significantly and extends across most of the plotted window, and this effect is even more pronounced for $\theta = 60°$. The corresponding exit-basin maps confirm that increasing tilt reduces leakage from the stable band and restores a large bounded region. A similar behavior is observed around L_5, so the corresponding maps are omitted here for brevity, as they do not introduce additional qualitative features beyond those already discussed for L_4.

This behavior indicates that the destabilizing effect of the purely radial positive-current forcing can be partly compensated by reorienting the tether. In other words, tilt acts here as a control parameter that redistributes the Lorentz acceleration in a more favorable way for preserving finite-time bounded motion near the triangular equilibria.

4.3.3 *Global stability and transport structure*

At the global scale, changing the tether tilt does not modify the main transport topology of the Earth–Moon CR3BP. For all three angles, the outer ring of long-lived ridges, the Moon-side lobe, and the central Earth-impact region remain in approximately the same locations. This confirms that tilt does not create new large-scale transport channels.

The main visible effect of tilt is a progressive fragmentation of the Earth-centered ring, particularly evident in the exit-basin maps. As the tilt angle increases, the inner band breaks into a more irregular and chaotic pattern, with increasingly intricate basin boundaries. This effect is already noticeable at $\theta = 30°$ and becomes more pronounced at $\theta = 60°$. A possible explanation is that tilting the tether redistributes the Lorentz acceleration between radial and along-track directions, reducing its alignment with the underlying manifold structure and enhancing transverse dispersion. As a result, trajectories

experience stronger mixing within the inner region, leading to a loss of coherence and a more complex basin structure. Even so, the bounded region remains much smaller than in the unforced case, and the global response should therefore be interpreted as a reweighting of the existing transport pathways rather than a restoration of the original CR3BP stability picture.

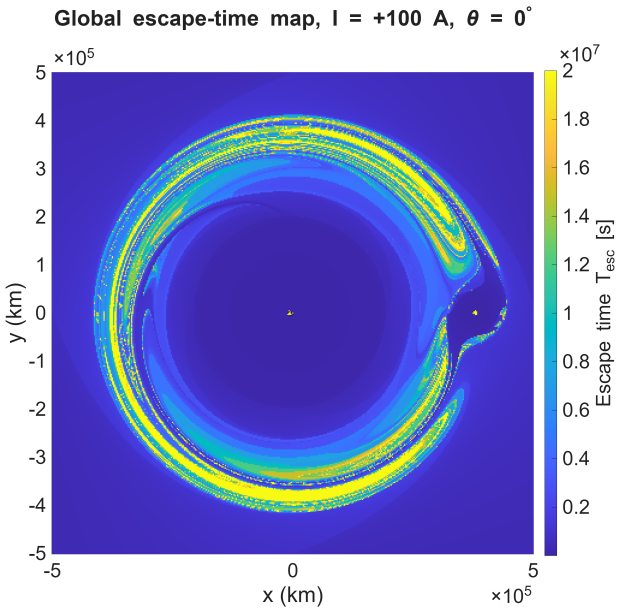

(a) Escape-time map

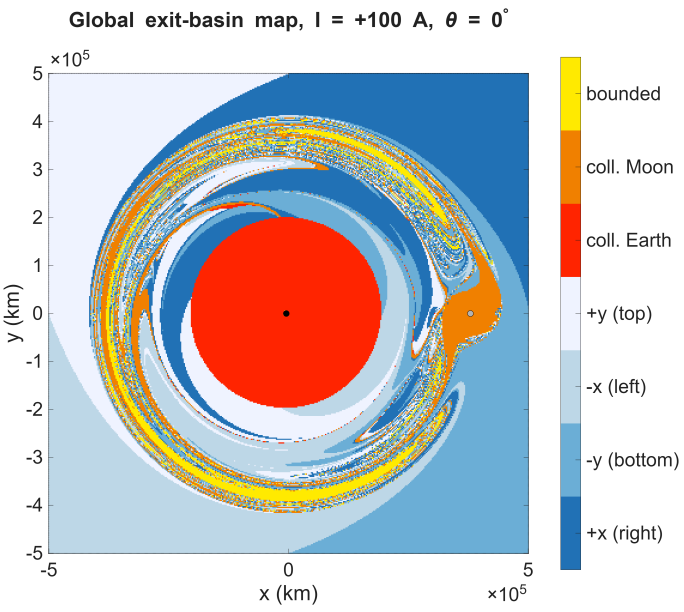

(b) Exit-basin map

Fig. 24 Global maps for $I = +100$ A, $\theta = 0°$.

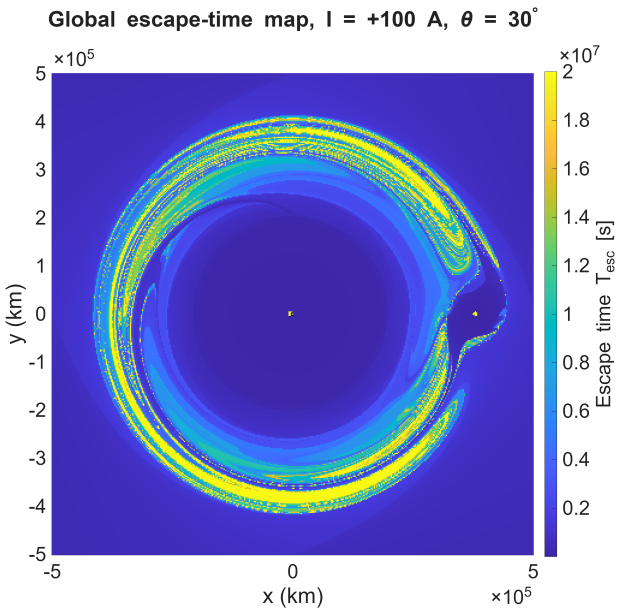

(a) Escape-time map

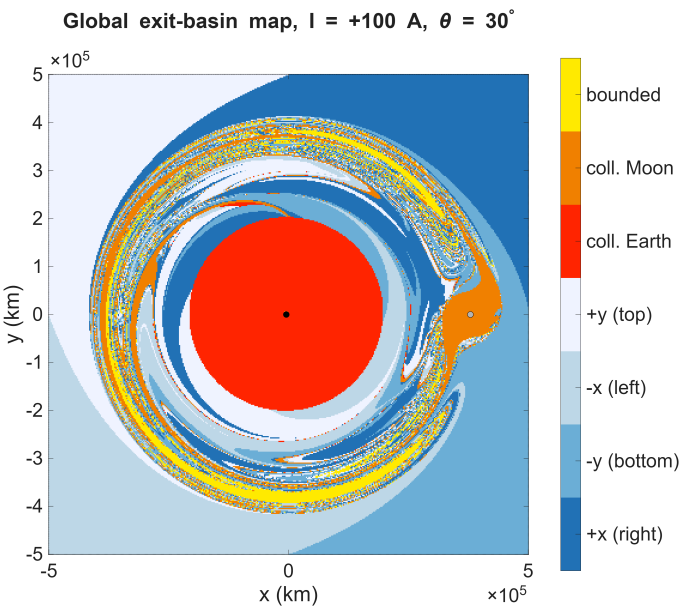

(b) Exit-basin map

Fig. 25 Global maps for $I = +100$ A, $\theta = 30°$.

Taken together, the tilt study shows that reorienting the tether has a weaker effect than changing the current polarity on the global topology, but it can still modify the local accessibility of long-lived regions. Its influence is most useful near the triangular points, where increasing tilt can partially recover bounded motion that is reduced in the purely radial forced case. More generally, tilt provides a secondary control parameter for shaping residence times and leakage rates without altering the overall transport skeleton of the Earth–Moon system.

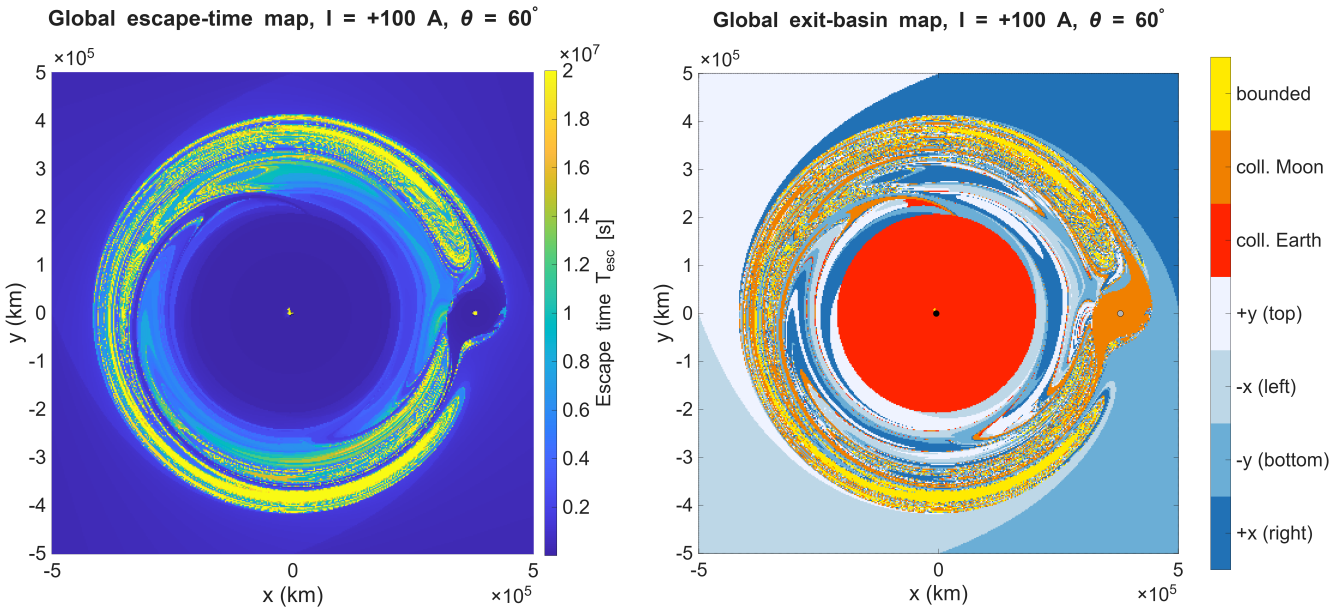

(a) Escape-time map **(b) Exit-basin map**

Fig. 26 Global maps for $I = +100$ A, $\theta = 60°$.

5 Conclusions and Future Work

This work investigated how Lorentz forcing from an electrodynamic tether modifies finite-time stability and transport in the planar Earth–Moon CR3BP through local and global escape-time and exit-basin maps. The results show that EDT actuation does not create a new large-scale transport topology, but it does significantly redistribute residence times and escape outcomes across the domain. The observed effects arise from the interaction between the Lorentz acceleration and the underlying CR3BP dynamics, together with the spatial variation of the dipole magnetic field, which is strongest near the Earth.

For the radial tether configuration, the response depends strongly on current polarity. Near the collinear points, the long-lived ridge around L_1 is strengthened for positive current and weakened for negative current, while the effect around L_2 is qualitatively similar but more modest. Around L_3, the forcing displaces and diffuses the thin long-lived strip in a sign-dependent way, indicating that the Lorentz term mainly biases access to an already existing transport structure rather than generating a new one. At the triangular points, the effect is much stronger: the broad stable bands around L_4 and L_5 are substantially eroded, and the regions of bounded motion become highly polarity-dependent.

The global maps confirm that the outer ring of long-lived ridges and the Moon-side lobe remain approximately in place under forcing, so the overall CR3BP transport skeleton is preserved. However, the broad Earth-centered bounded ring of the unforced problem is strongly reduced. Negative current mainly redirects trajectories toward Earth impact, whereas positive current increases the accessibility of the pre-existing escape channels and allows many trajectories that were bounded in the unforced case to escape. In this sense, EDT forcing acts primarily as a mechanism for reweighting transport pathways over time.

The tilt study shows that reorienting the tether provides a secondary but useful control parameter. Its influence is limited around L_2, reduces bounded motion near L_1, and increases the maximum escape time along the thin long-lived strip near L_3, suggesting a more favorable alignment of the Lorentz acceleration with that structure. The most beneficial effect of tilt appears near the triangular points, where increasing θ partially restores bounded motion that is lost in the purely radial positive-current case. At the global scale, tilt does not alter the main transport topology, but it makes the Earth-centered inner ring progressively

more fragmented and irregular, particularly in the exit-basin maps, consistent with stronger mixing and more intricate basin boundaries.

Overall, the results indicate that EDT actuation in the Earth–Moon CR3BP is better interpreted as a transport-shaping mechanism than as a means of creating new stable regions. Current polarity is the dominant parameter controlling whether trajectories are driven toward impact or escape, while tether tilt can locally enhance or suppress leakage depending on the geometry of the underlying invariant structures. This suggests that EDTs could provide a low-thrust, propellantless means of modulating residence times and transport accessibility in cislunar space.

The present model remains intentionally simplified. The dynamics are restricted to the planar CR3BP, the magnetic field is represented through a uniform, leading-order aligned-dipole approximation, and the tether is modeled as a rigid conductor with constant current and lumped mass. Out-of-plane motion, solar perturbations, higher-order terrestrial gravity harmonics, realistic plasma-current collection, and tether structural dynamics are neglected. Natural extensions of this work include a fully three-dimensional formulation, coupling the current to EMF and plasma-interaction models, and studying time-varying current and tilt laws as control inputs for station-keeping, leakage mitigation, or transfer design near cislunar libration regions.

Declaration of Use of Artificial Intelligence

Generative AI was used as a complementary tool to improve efficiency and clarity without replacing the original research. ChatGPT (versions 4 and 5), CODEX and MATLAB Copilot assisted with text refinement, reference formatting, MATLAB debugging, and figure preparation. These tools were also used to support edits in the presentation of figures and the wording of the manuscript. All outputs were reviewed and verified by the authors against authoritative sources.

References

[1] E. Lorenzini and J. Sanmartín, "Electrodynamic tethers in space," *Scientific American*, vol. 291, no. 2, pp. 50–57, Aug. 2004. [Online]. Available: https://www.jstor.org/stable/10.2307/26060646.

[2] H. Poincaré, *The Three-Body Problem and the Equations of Dynamics: Poincaré's Foundational Work on Dynamical Systems Theory* (Astrophysics and Space Science Library), trans. by B. D. Popp. Cham: Springer International Publishing, 2017, vol. 443. DOI: 10.1007/978-3-319-52899-1.

[3] R. A. Broucke, "Periodic orbits in the restricted three-body problem with earth–moon masses," NASA Jet Propulsion Laboratory, Pasadena, California, Tech. Rep. JPL Technical Report 32-1168, 1968, NASA Technical Report. [Online]. Available: chrome-extension://efaidnbmnnnibpcajpcglclefindmkaj/https://ntrs.nasa.gov/api/citations/19680013800/downloads/19680013800.pdf.

[4] R. W. Farquhar, *The Control and Use of Libration-Point Satellites*. 1970, Available from NASA Technical Reports Server. [Online]. Available: chrome-extension://efaidnbmnnnibpcajpcglclefindmkaj/https://ntrs.nasa.gov/api/citations/19710000821/downloads/19710000821.pdf.

[5] J. R. Sanmartín, E. C. Lorenzini, and M. Martinez-Sanchez, "A review of electrodynamic tethers for space applications," NASA, Tech. Rep., 2010, Universidad Politécnica de Madrid, University of Padova, and Massachusetts Institute of Technology.

[6] N. H. Stone, "Unique results and lessons learned from the TSS missions," in *Fifth International Conference on Tethers in Space*, Ann Arbor, Michigan: NeXolve Corporation, Inc., 2016, pp. 1–13.

[7] M. D. Grossi, "Plasma motor generator (PMG) electrodynamic tether experiment: Final report," Smithsonian Astrophysical Observatory, Cambridge, Massachusetts, Tech. Rep. NASA Grant NAG9-643, 1995.

[8] J. Ballance and L. Johnson, "Propulsive small expendable deployer system (ProSEDS)," in *Proceedings of the Space Technology and Applications International Forum (STAIF)*, Marshall Space Flight Center, Alabama: NASA Marshall Space Flight Center, 2000, pp. 1–6.

[9] J. Peláez et al., "Dynamics and stability of tethered satellites at lagrangian points," Advanced Concepts Team, European Space Agency (ESTEC), Tech. Rep., 2008.

[10] D. Zanutto, D. Curreli, and E. C. Lorenzini, "Stability of electrodynamic tethers in a three-body system," *Journal of Guidance, Control, and Dynamics*, vol. 34, no. 5, pp. 1441–1453, 2011. DOI: 10.2514/1.52755. [Online]. Available: https://doi.org/10.2514/1.52755.

[11] J. Liu, X. Zhan, G. Li, Q. Wang, and S. Wang, "Dynamics of orbital boost maneuver of low earth orbit satellites by electrodynamic tethers," *Aerospace Systems*, vol. 3, pp. 189–196, 2020. DOI: 10.1007/s42401-020-00053-y.

[12] M. S. Rivo, "Self balanced bare electrodynamic tethers: Space debris mitigation and other applications," Ph.D. dissertation, Escuela Técnica Superior de Ingenieros Aeronáuticos, Universidad Politécnica de Madrid, Madrid, Spain, 2009.

[13] M. Iñarrea, V. Lanchares, A. I. Pascual, and J. P. Salas, "Attitude stabilization of electrodynamic tethers in elliptic orbits by time-delay feedback control," *Acta Astronautica*, vol. 96, pp. 280–295, 2014. DOI: 10.1016/j.actaastro.2013.12.011.

[14] E. Velasco, *Mapping of stability zones for electrodynamic tethers in a circular restricted three-body system using lagrange points*, Bachelor's Thesis, Supervised by Behrad Vatankhahghadim, 2025.

[15] A. H. J. de Ruiter, C. J. Damaren, and J. R. Forbes, *Spacecraft Dynamics and Control: An Introduction*. Chichester, West Sussex, UK: John Wiley & Sons, Ltd., 2013.

[16] G. W. Hill, "Researches in the lunar theory," *American Journal of Mathematics*, vol. 1, no. 1, pp. 5–26, 1878.

[17] W. S. Koon, M. W. Lo, J. E. Marsden, and S. D. Ross, *Dynamical Systems, the Three-Body Problem and Space Mission Design*. Marsden Books, 2011, Available online: https://www2.hawaii.edu/~koon/book/.

[18] V. Szebehely, *Theory of Orbits: The Restricted Problem of Three Bodies*. New York and London: Academic Press, 1967.

[19] J. Aguirre, R. L. Viana, and M. A. F. Sanjuán, "Fractal structures in nonlinear dynamics," *Reviews of Modern Physics*, vol. 73, no. 1, pp. 137–162, 2001. DOI: 10.1103/RevModPhys.73.137.

[20] J. R. Sanmartín, A. Sánchez-Torres, S. B. Khan, G. Sánchez-Arriaga, and M. Charro, "Optimum sizing of bare-tape tethers for de-orbiting satellites at end of mission," *Acta Astronautica*, vol. 95, pp. 206–217, 2014. DOI: 10.1016/j.actaastro.2013.10.010.